

CHAPTER FOUR

MICROBURST SIZE DISTRIBUTION DERIVED WITH AEROCUBE-6

Contribution of Authors and Co-Authors

Manuscript(s) in Chapter(s) 1

Author: [type author name here]

Contributions: [list contributions here, single-spaced]

Co-Author: [type co-author name here]

Contributions: [list contributions here, single-spaced]

Co-Author: [type co-author name here]

Contributions: [list contributions here, single-spaced]

13

Manuscript Information

14 [Type Author and Co-author(s) Names Here]

15 Journal of Geophysical Research

16 Status of Manuscript: Officially submitted to a peer-reviewed journal

17 Wiley

18

Key Points

19

- 20 • The dual AeroCube-6 CubeSats simultaneously observed > 35 keV microbursts
21 at a variety of spatial separations ranging from 2 to ≈ 100 km.
- 22 • In low Earth orbit the majority of microbursts have a size on the order of a few
23 tens of km.
- 24 • At the magnetic equator, the size of most microbursts corresponds to the size
25 of whistler-mode chorus wave packets.

Abstract

26

27 Microbursts are an impulsive increase of electrons from the radiation belts
28 into the atmosphere and have been directly observed in low Earth orbit and the
29 upper atmosphere. Prior work has estimated that microbursts are capable of rapidly
30 depleting the radiation belt electrons on the order of a day, hence their role to
31 radiation belt electron losses must be considered. Losses due to microbursts are not
32 well constrained, and more work is necessary to accurately quantify their contribution
33 as a loss process. To address this question we present a statistical study of > 35
34 keV microburst sizes using the pair of AeroCube-6 CubeSats. The microburst size
35 distribution in low Earth orbit and the magnetic equator was derived using both
36 spacecraft. In low Earth orbit, the majority of microbursts were observed while the
37 AeroCube-6 separation was less than a few tens of km, mostly in latitude. To account
38 for the statistical effects of random microburst locations and sizes, a Monte Carlo and
39 analytic models were developed to test hypothesized microburst size distributions. A
40 family of microburst size distributions were tested and a Markov Chain Monte Carlo
41 sampler was used to estimate the optimal distribution of the microburst size model

parameters. Finally, a majority of observed microbursts map to sizes less than 200 km at the magnetic equator. Since microbursts are widely believed to be generated by scattering of radiation belt electrons by whistler mode waves, the observed microburst size correlates to coherent whistler mode chorus sizes derived in prior literature.

Introduction

Since the discovery of the Van Allen radiation belts in the 1960s by Van Allen (1959) and Vernov and Chudakov (1960), decades of research has made headway in understanding the various particle acceleration and loss mechanisms. One of the extensively studied mechanisms responsible for both acceleration and loss is wave-particle scattering between whistler-mode chorus waves and electrons (Abel and Thorne, 1998; Bortnik et al., 2008; Horne and Thorne, 2003; Meredith et al., 2002; Millan and Thorne, 2007; Thorne et al., 2005). Whistler-mode chorus waves are typically generated by a temperature anisotropy of low energy electrons up to tens of kiloelectronvolts (keV) and are typically found in the $\sim 0 - 12$ magnetic local times (MLT) (Li et al., 2009a,b). Whistler-mode chorus waves interact with radiation belt electrons, and are widely believed to cause electron precipitation termed microbursts (e.g. Millan and Thorne, 2007).

Microbursts are a subsecond impulse of electrons that are observed by high altitude balloons and satellites in low Earth orbit (LEO) on radiation belt magnetic footprints $\sim 4 - 8$ L-shell (L) (e.g. Anderson and Milton, 1964; Breneman et al., 2017; Crew et al., 2016; Greeley et al., 2019; Lorentzen et al., 2001a; Mozer et al., 2018; O'Brien et al., 2003; Tsurutani et al., 2013; Woodger et al., 2015), mostly in the dawn MLTs, and with an enhanced occurrence rate during disturbed magnetospheric times (Douma et al., 2017; O'Brien et al., 2003). Microburst's role as a radiation belt electron loss mechanism has been estimated to be significant, with total radiation belt

67 electron depletion due to microbursts estimated to be on the order of a day (Breneman
 68 et al., 2017; Lorentzen et al., 2001b; O’Brien et al., 2004; Thorne et al., 2005). These
 69 average microburst loss estimates are not well constrained due to assumptions made
 70 regarding the microburst precipitation region.

71 One of the unconstrained microburst parameters that is critical to better
 72 quantify the role of microbursts as an instantaneous loss mechanism (the number
 73 of electrons lost per microburst) is their physical size. Historically, after the
 74 bremsstrahlung X-ray signatures of microbursts were discovered by Anderson and
 75 Milton (1964), numerous microburst size studies were done using other balloon flights
 76 in the mid 1960s. Brown et al. (1965) used data from a pair of balloons separated
 77 by 150 km, mainly in longitude, and found that one third of all microbursts observed
 78 were temporally coincident. Trefall et al. (1966) then used the results from Brown
 79 et al. (1965) to model the probability that a microburst will be observed by two
 80 balloons as a function of the radius of the microburst, radius of the precipitating area
 81 a balloon is sensitive to, and the balloon separation. Trefall et al. (1966) concluded
 82 that the microbursts reported by Brown et al. (1965) must have had a diameter of
 83 230 km assuming a balloon has a circular field of view with a 140 km diameter (for
 84 electrons stopped at 100 km altitudes). Soon after, Barcus et al. (1966) used a pair of
 85 balloons and concluded that a microburst must have a < 200 km longitudinal extent.
 86 Then Parks (1967) used data from a single balloon with four collimated scintillators
 87 oriented in different directions and found that the size of some mostly low energy
 88 microbursts to have a diameter of 80 ± 28 km, and others were less than 40 km.

89 Direct observations of microburst electrons are made by LEO spacecraft. Blake
 90 et al. (1996) found a microburst with a size of a few tens of km using the the Solar
 91 Anomalous and Magnetospheric Particle Explorer (SAMPEX) and concluded that
 92 typically microbursts are less than a few tens of electron gyroradii in size (order of

93 a few km in LEO). Recently, Dietrich et al. (2010) used SAMPEX observations in
 94 another case study and concluded that the observed microbursts were smaller than 4
 95 km. Crew et al. (2016) used the Focused Investigation of Relativistic Electron Bursts:
 96 Intensity, Range, and Dynamics (FIREBIRD-II) CubeSats and found an example of
 97 a microburst larger than 11 km. Lastly, Shumko et al. (2018) also used FIREBIRD-II
 98 to identify a microburst with a size greater than 51 ± 1 km. If anything, the large
 99 variance in prior results imply that there is a distribution of microburst scale sizes
 100 which this study aims to estimate.

101 Besides addressing the instantaneous radiation belt electron losses due to
 102 individual microbursts, the microburst size distribution is useful to identify the wave
 103 mode(s) responsible for scattering microbursts. By mapping the microburst size
 104 distribution in LEO to the magnetic equator it can be compared to the wave sizes
 105 estimated in prior literature. This comparison can be used to identify the waves and
 106 their properties (e.g. amplitude or coherence) responsible for scattering microburst
 107 electrons.

108 This paper addresses these two questions by expanding the prior microburst
 109 size case studies by analyzing microburst observations over a three year time period
 110 to estimate the microburst size distribution in LEO and the magnetic equator. The
 111 twin AeroCube-6 (AC6) CubeSats are utilized for this study because they were ideally
 112 equipped to observe microbursts simultaneously over a span of three years while their
 113 total separation varied between 2 and 800 km, mostly in latitude (in-track in orbit).
 114 This paper first describes the AC-6 mission, including their orbit and instrumentation
 115 in section 1. Section 1 develops the methodology used to identify microbursts observed
 116 by each spacecraft and how they were combined to make a list of simultaneously
 117 observed microbursts. Section 1 describes the methodology used to estimate the
 118 microburst size distributions in LEO and the magnetic equator as a function of AC6

119 separation. Then a model is developed to shed light on how the compounding effects of
 120 a hypothesized microburst shape, size distribution, and random microburst locations
 121 will be observed by AC6, a two-point measurement platform. Lastly, in section 1
 122 we discuss these results and compare the microburst sizes estimated here to the size
 123 distribution of the whistler-mode chorus waves that are believed to cause microbursts.

124 Instrumentation

125 The AC6 mission consists of a pair of 0.5U (10x10x5 cm) CubeSats built by
 126 The Aerospace Corporation and launched on June 19th, 2014 into a 620 x 700 km,
 127 98° inclination orbit. The two satellites, designated as AC6-A and AC6-B, separated
 128 after launch and drifted apart. Both AC6 units have an active attitude control system
 129 which allows them to adjust the atmospheric drag experienced by each AC6 unit by
 130 orienting their solar panel “wings” with respect to the ram direction. By changing
 131 their orientation, AC6 was able to achieve fine separation control and maintain a
 132 separation between 2-800 km. Figure 1.1a shows the AC6 separation for the duration
 133 of the mission. Figure 1.1b shows where AC6 was taking 10 Hz data simultaneously
 134 as a function of L and MLT which highlights that most data was taken at 8-12 MLT,
 135 an ideal local time for observing microbursts. Lastly Fig. 1.1b shows that the AC6
 136 orbit was roughly dawn-dusk, sun-synchronous and precessed only a few hours in
 137 MLT over a three year period.

138 Each AC6 unit is equipped with three Aerospace microdosimeters (licensed to
 139 Teledyne Microelectronics, Inc). The dosimeter used for this study is dos1 and is
 140 identical on both AC6 units. Dos1 has a 35 keV electron threshold and all dosimeters
 141 sample at 1 Hz in survey mode, and 10 Hz in burst mode in the radiation belts. More
 142 detailed technical information on AC6 is described in O’Brien et al. (2016).

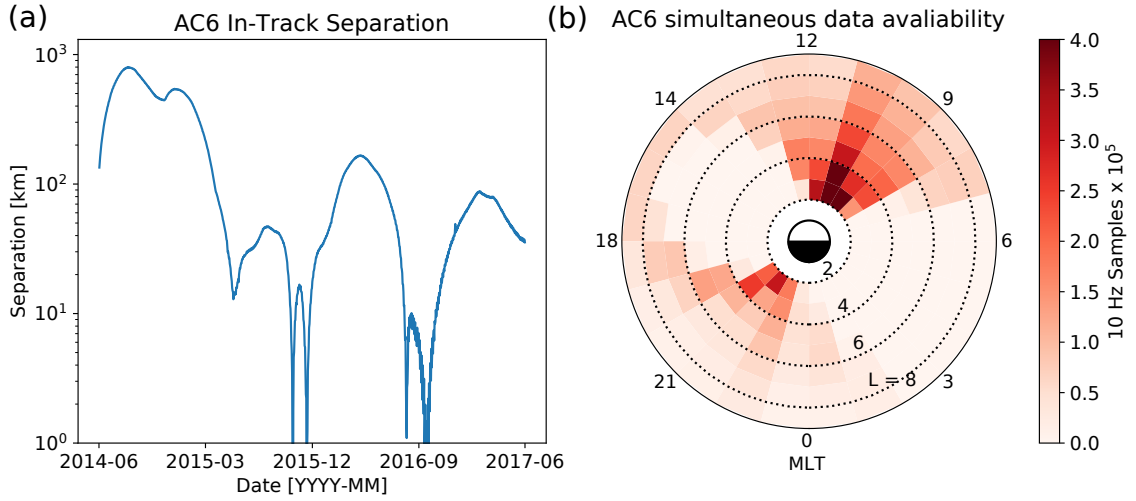


Figure 1.1: AC6 mission properties for (a) spacecraft separation and (b) number of simultaneous quality 10 Hz samples as a function of L and MLT.

143

Methodology

Microburst Detection

The first step to find microbursts observed simultaneously by AC6 is to identify them on each individual spacecraft. Microbursts were detected with two different methods that yielded quantitatively similar results. The first method is the burst parameter (O'Brien et al., 2003). This algorithm has been successfully used in other microburst studies, mainly with the microbursts observed by SAMPEX (e.g. Blum et al., 2015; Douma et al., 2017; O'Brien et al., 2003). For AC6, a burst parameter threshold of 5 was determined to be a good trade-off between false positive and false negative microburst detections. Another microburst detection algorithm based on wavelet spectra frequency filtering was developed and the resulting list of microbursts is similar to the list from the burst parameter.

With the two microburst detection lists in hand, data cleaning to remove microburst-like transmitter noise was necessary. The transmitters on AC6 can

155

156

157 cause unphysical count impulses in the dosimeters that resembles periodic trains of
 158 microbursts. One source of transmitter noise was observed at times when AC6 was in
 159 contact with the ground stations above the US for data downloads and commanding,
 160 thus the microburst detections made above the US that were mostly at low L were
 161 discarded.

162 Another source of noise is crosslink transmissions between AC6-A and AC6-B.
 163 These transmissions occurred when either spacecraft transitioned from the survey
 164 mode to 10 Hz mode. This noise is sometimes not caught by the data quality flag, so
 165 the following empirically-derived criteria were developed to remove those detections.
 166 The dosimeter with a 250 keV nominal electron threshold, dos2, was used because it
 167 had a nearly identical response to noise while rarely responded to microbursts. Since
 168 the transmitter noise is very periodic with a ≈ 0.2 s period, cross-correlation (CC)
 169 and autocorrelation (AC) methods were applied to the dos1 and dos2 time series.
 170 Detections were discarded if the following two criteria were met: either dos1 or dos2
 171 time series had a AC peak at a 0.2 or 0.4 s lag and the dos1-dos2 CC was greater
 172 than 0.9. The AC lag criteria alone sometimes falsely removed legitimate trains of
 173 microbursts, so the second criteria insured that the detection was removed if there
 174 was also an unphysically high correlation across an order of magnitude in energy.

175 The lists of microbursts observed individually by AC6 were then merged into
 176 a list of temporally correlated microbursts, i.e. microbursts that were observed
 177 simultaneously by both AC6 units, with the following procedure. The general idea is
 178 that a microburst detected by one spacecraft will cross-correlate well with the time
 179 series from the other spacecraft if it observed a similar microburst, and poorly if
 180 there was no microburst observed by the other spacecraft. Each microburst detection
 181 made by either spacecraft was cross-correlated with the time series from the other
 182 spacecraft whether or not a microburst was observed by the other spacecraft. Cross-

correlation windows with 1 and 1.2 s widths were chosen with slightly different window sizes to account for random count variation due to Poisson noise. Microbursts detections that had a cross-correlation greater than 0.8 were considered temporally coincident. This CC threshold was chosen as it is low enough to accept user-identified temporally coincident microbursts superposed with noise, and high enough to reject most non-coincident events. Figure 1.2, panels (a), (c), (e), and (g) show examples of microbursts observed by both AC6 units when they were separated by 5, 16, 37, and 69 km, respectively.

The last criteria requires that the temporal CC must be greater than the spatial CC + 0.3. The spatial CC was calculated by shifting one spacecraft's time series by the in-track lag to cross-correlate in the same spatial location, i.e. latitude. This criteria was applied to remove curtains, stationary structures observed by AC6 that are narrow in latitude (Blake and O'Brien, 2016) that can be misidentified as microbursts. Figure 1.2, panels (b), (d), (f), and (h) show the shifted time series to confirm that there were no spatially correlated, non-microburst structures present. Lastly the merged microburst list was spot checked by two authors to remove poorly correlated and any duplicate events. After filtering out transmitter noise and applying the CC criteria, 662 simultaneous microburst detections were found and used in this study.

Microburst Size Distribution in LEO and Magnetic Equator

The temporally coincident microbursts, which from now on will be referred to as microbursts, are now used to estimate the fraction of microbursts observed above AC6 separation, s . When AC6 observes a microburst at s , the microburst's size must be greater than s . This fact, along with the arguments presented in Section 4 in Joy et al. (2002) who studied the most probable Jovian magnetopause and bow

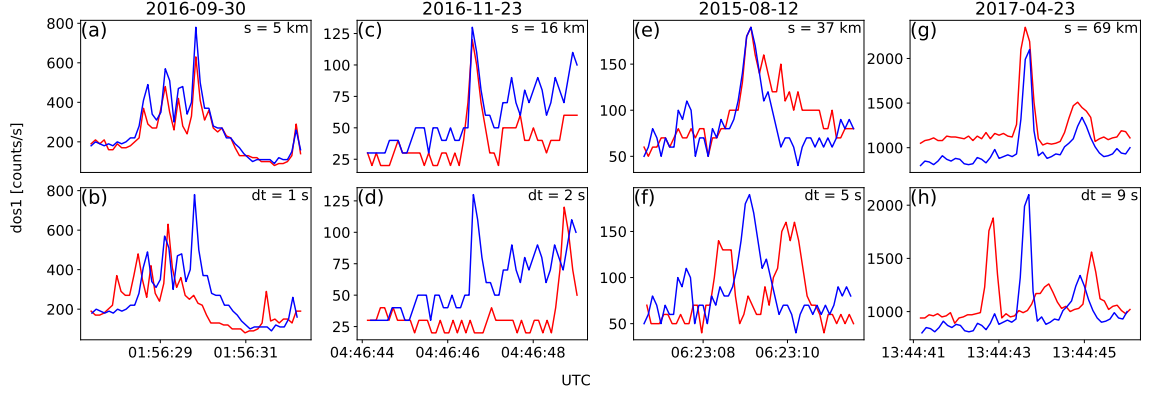


Figure 1.2: Examples of > 35 keV microbursts observed simultaneously by AC6-A in red and AC6-B in blue. Panels (a), (c), (e), and (g) show the temporally-aligned time series when AC6 were separated by $s = 5, 16, 37$, and 69 km, respectively. The corresponding panels (b), (d), (f), and (h) show the spatially-aligned time series which is made by shifting the AC6-A time series in the above panels by the in-track lag (annotated with dt) that show any spatially correlated structures. The clear temporal correlation and lack of spatial correlation demonstrates that these events are microbursts.

shock stand off distances, are used to investigate the dependence of the number of
microbursts observed above s , as a function of s . This dependence is the microburst
complementary cumulative distribution function $\bar{F}(s)$.

The cumulative fraction of microbursts observed above s is the ratio of $N(s)$,
the normalized number of microbursts observed above s , to $N(0)$, the total number
of microbursts observed

$$\bar{F}(s) = \frac{N(s)}{N(0)} \quad (1.1)$$

where $N(s)$ is defined by

$$N(s) = \sum_{i=s}^{\infty} n_i \left(\frac{S_{max}}{S_i} \right) \quad (1.2)$$

where n_i is the number of microbursts observed by AC6 in i th separation bin.

The normalization term S_{max}/S_i is a ratio of the number of 10 Hz samples in

the most sampled separation bin to the number of samples in the i th bin. This normalization factor corrects AC6's non-uniform sampling in separation, thus $\bar{F}(s)$ can be interpreted as the fraction of microbursts observed above s assuming AC6 sampled evenly in separation. Microburst $\bar{F}(s)$ in LEO is shown by the black curve in Fig. 1.3a for $4 < L < 8$ and split into one L -wide bins with the colored curves. The separation bin width used in Fig. 1.3 is 5 km. To check for bias in $\bar{F}(s)$ due to the choice of separation bins, $\bar{F}(s)$ was resampled using other bin widths and offsets. Bin widths as large as 20 – 30 km and bin offsets did not qualitatively effect the curves in Fig. 1.3a. The normalization i.e., the number of 10 Hz samples in each separation bin, is shown in 1.3c.

The overall trend in Fig. 1.3a shows a sudden cumulative probability drop off, followed by a shoulder up to $s \approx 70$ km where $\bar{F}(s)$ drops to nearly zero. A large negative gradient of $\bar{F}(s)$ at some separation implies that microbursts must be smaller than that separation. To quantify this, Fig. 1.3b shows the microburst probability density function (PDF), calculated by differentiating $\bar{F}(s)$. The microburst PDF shows a peak at $s < 30$ km as well as a peak between 70 – 80 km separation. These PDF peaks are evidence of a sub 30 km microburst population and larger microbursts observed up 70–80 km separations. The shaded region around the black curves in Fig. 1.3a-b shows the standard error due to counting statistics. The uncertainty due to false coincidence events i.e. two unrelated microbursts lining up in time by random chance was also considered. The microburst duty cycle in a one minute window ($\approx 1 L$) around each microburst was calculated. The false coincidence probability is the square of the duty cycle and was found to be less than 5% for the majority of microbursts. The false coincidence probability for each microburst was then used to randomly remove microbursts and $\bar{F}(s)$ was recalculated in 10^4 trials. The spread in the $\bar{F}(s)$ trial curves with microbursts randomly removed was much smaller than the

240 uncertainty due to counting statistics alone.

241 To compare the microburst size to the size of their hypothesized progenitor
 242 waves, the spacecraft locations during observed microbursts were mapped to the
 243 magnetic equator using the Olson-Pfitzer magnetic field model (Olson and Pfitzer,
 244 1982) which is implemented with a Python wrapper for IRBEM-Lib (Boscher et al.,
 245 2012). As previously stated, a microburst observed in LEO has a size larger than
 246 the spacecraft separation, hence that microburst would also have a size larger than
 247 the spacecraft separation after it was mapped to the magnetic equator. Thus
 248 the procedure to estimate $\bar{F}(s)$ is identical to the LEO size distribution but with
 249 a different normalization. The normalization factors were calculated by mapping
 250 every quality AC6 sample to the magnetic equator and binning them by equatorial
 251 separation into 100 km wide bins. Figure 1.4 shows the equatorial microburst size
 252 distribution in the same format as Fig. 1.3. The equatorial PDF trend is similar to
 253 LEO and most of the microbursts were observed when the AC6 equatorial separation
 254 was less than 200 km.

255 The results in Figs. 1.3 and 1.4 show the fraction of microbursts observed above a
 256 spacecraft separation and do not fully represent the microbursts size distribution due
 257 to the compounding effects from the range of microburst sizes and random locations
 258 of microbursts with respect to AC6 i.e. even if the microburst size is much larger than
 259 the AC6 separation, some fraction of those microbursts will be only observed by one
 260 AC6 spacecraft. Thus modeling is necessary to capture the compounding influence
 261 of these statistical effects on AC6.

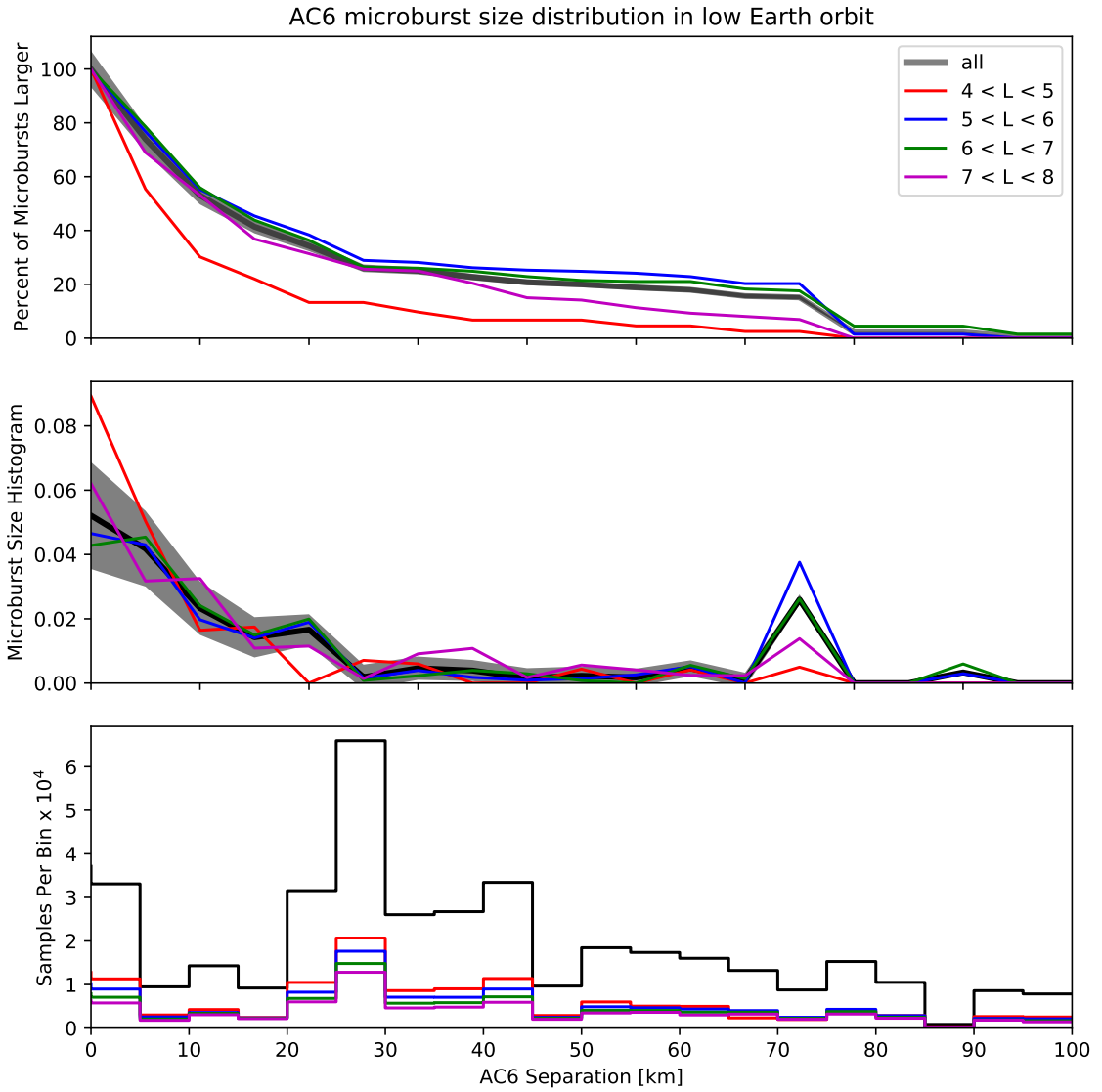


Figure 1.3: Microburst size distribution in low Earth orbit. Panel (a) shows the percent of microbursts observed above that separation after normalizing for the uneven AC6 sampling in separation. Panel (b) shows the microburst probability density (size histogram) as a function of separation. Lastly, panel (c) shows the normalization, i.e. number of simultaneous samples AC6 observed as a function of separation. The colored lines show the distributions binned by L , and the thick black curve for the entire radiation belt ($4 < L < 8$). The gray shading around the black curve shows the uncertainty due to counting statistics.

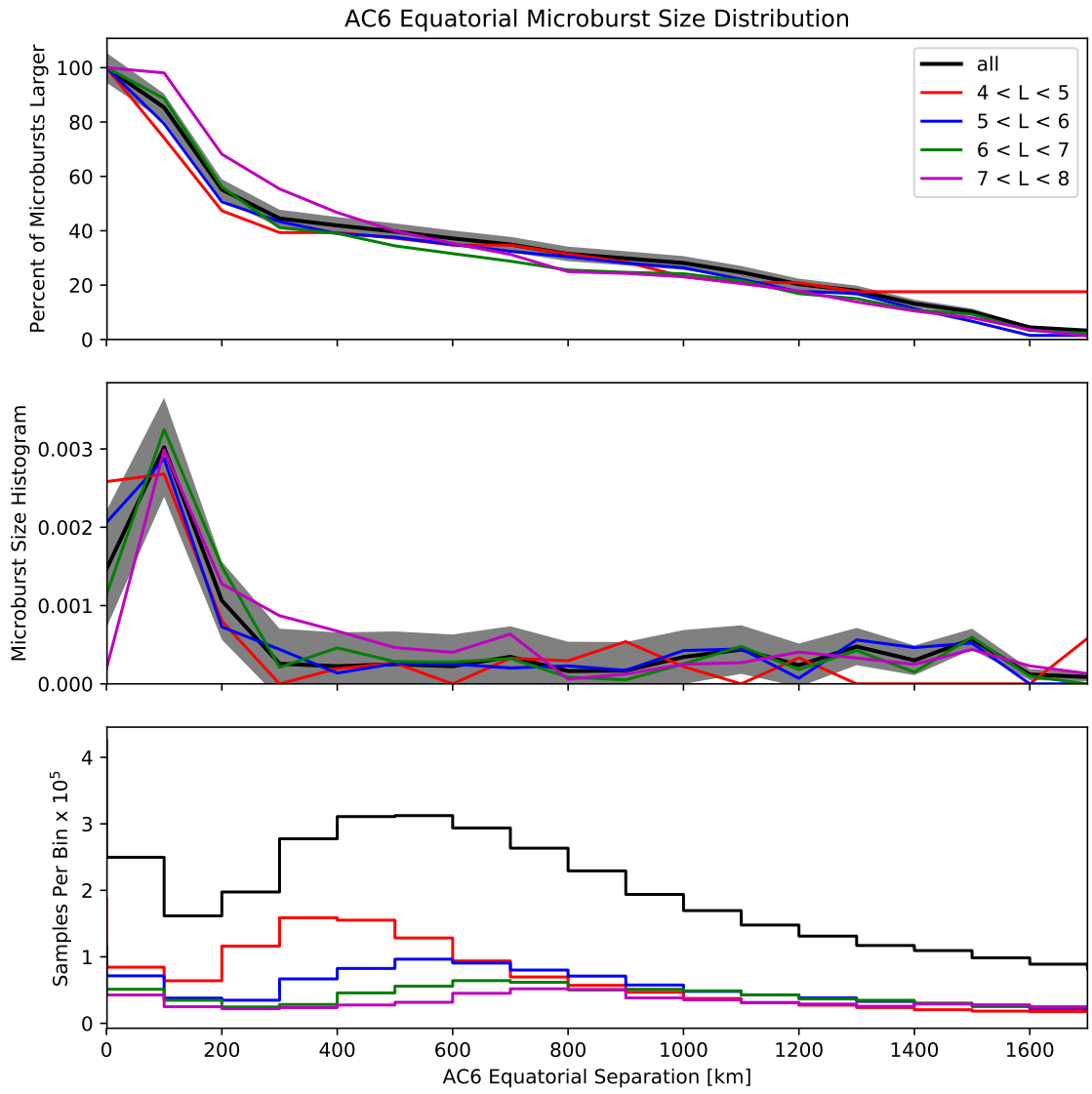


Figure 1.4: Microburst size distribution mapped to the magnetic equator in the same format as Fig. 1.3.

Modeling the Distribution of Microburst Sizes

Monte Carlo and Analytic Models to Calculate $\bar{F}(s)$

To account for the effects due to microbursts randomly occurring around AC6 with an unknown distribution of microburst sizes, Monte Carlo (MC) and analytic models were developed. These models assume a hypothesized distribution of microburst sizes expressed with a probability density function $p(d|\theta)$ where θ are the dependent variables, and a microburst footprint shape to estimate $\bar{F}(s)$. The microburst footprint is assumed to be circular with a diameter d . $p(d|\theta)$ can be understood as “the probability of observing a microburst of diameter d , given the parameters θ ”. Various microburst size distributions were considered: a one-size and two-size microburst populations, and continuous $p(d|\theta)$ such as Maxwell, Weibull, and log-normal.

The Monte Carlo model is the most intuitive. It first randomly scatters 10^5 microburst centers in a 400 x 400 km grid around AC6. Then each microburst center was assigned a diameter, randomly picked from a $p(d|\theta)$ distribution after θ parameters were specified. Spacecraft A is placed at the origin, and spacecraft B is placed along the positive y-axis at distances from spacecraft A corresponding to the AC6 separation bins used in Section 1. Then for each spacecraft B location, the number of microbursts that encompass both spacecraft was counted. The modeled fraction of microbursts observed above s is then

$$\bar{F}(s) = \frac{\sum_{i>s}^{\infty} n_i}{\sum_{i>0}^{\infty} n_i}. \quad (1.3)$$

where as before the number of microbursts observed by both spacecraft in the i th bin

283 is n_i .

The analytic model, while identical to the MC model, highlights the geometrical concepts connecting $p(d|\theta)$ and $\bar{F}(s)$ with geometry arguments similar to Trefall et al. (1966). For a microburst with $d = 2r \geq s$, there is an area between AC6 where that microburst will be observed by both spacecraft if the microburst's center lands there. Figure 1.5a-c shows this geometry with the two spacecraft indicated with black dots with varying relations between r and s . All microbursts whose center lies inside the circular area of radius r surrounding either spacecraft will be observed by that spacecraft. If it exists, the intersection of the two circular areas around both spacecraft defines another area, $A(r, s)$ where a microburst will be observed by both spacecraft if the microburst center lands there. This area can be calculated using the circle-circle intersection area equation,

$$A(r, s) = 2r^2 \cos^{-1} \left(\frac{s}{2r} \right) - \frac{s}{2} \sqrt{4r^2 - s^2}. \quad (1.4)$$

284 Example geometries where $A(r, s) > 0$ are shown in Fig. 1.5b and c. With this
 285 conceptual model and $A(r, s)$, the analytic form of $\bar{F}(s)$ can be found and is derived
 286 in the Supporting Information (SI) Text S1. To demonstrate the effects of random
 287 microburst locations near AC6, examples of the analytic and Monte Carlo $\bar{F}(s)$ curves
 288 are shown in Fig. 1.5d for a one-size, $d = 40$ km microburst population.

289 Methods for estimating optimal θ parameters

290 At this stage we have all of the ingredients to calculate $\bar{F}(s)$ given a prescribed
 291 $p(d|\theta)$. For each $p(d|\theta)$ tested, the optimal θ parameters are estimated in this study
 292 using the traditional least squares regression and Bayesian inference. While we
 293 report the θ parameters that minimize least squares, this section focuses on Bayesian
 294 inference because it seamlessly incorporates statistical uncertainty in the data. The

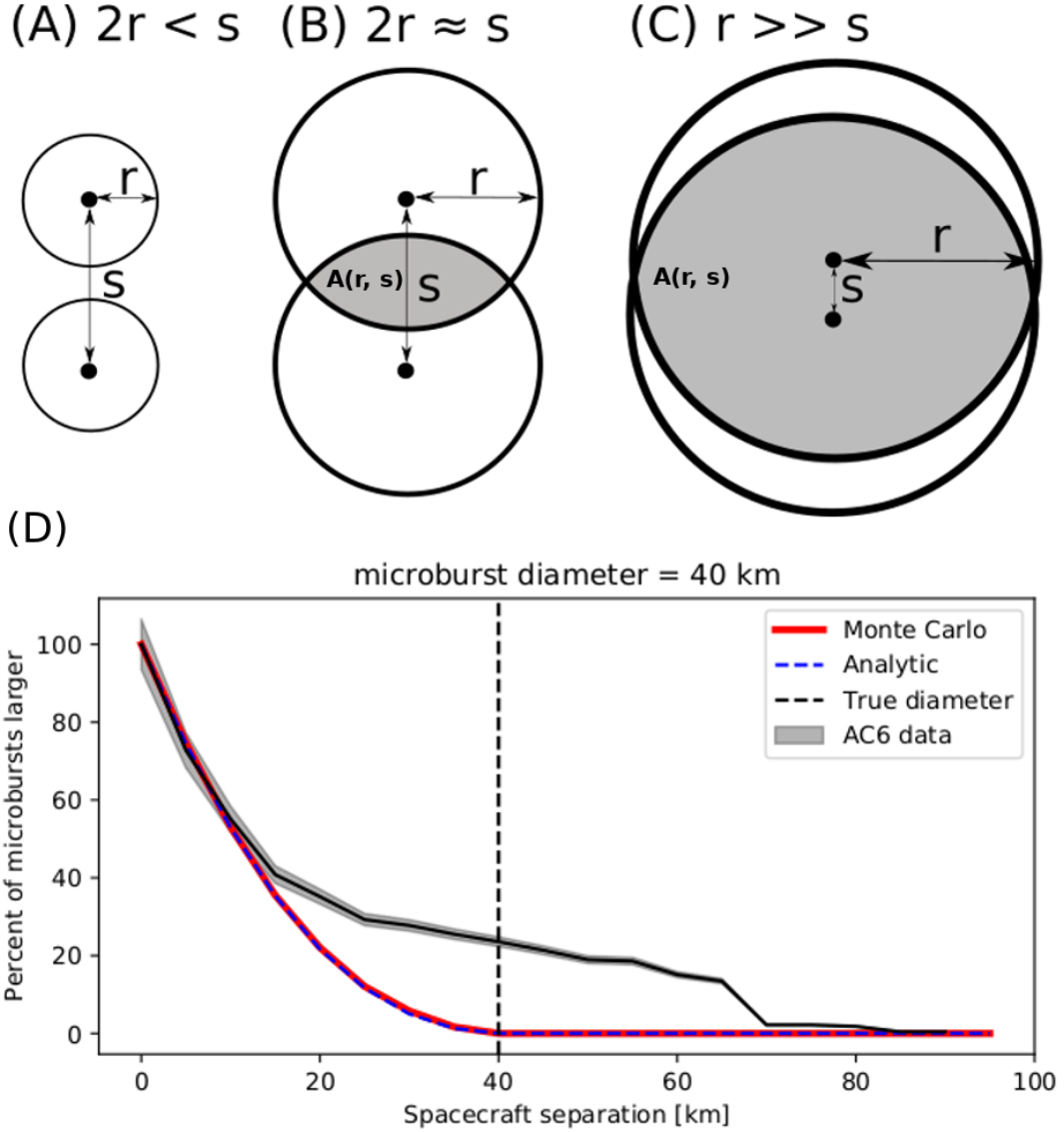


Figure 1.5: Panels A-C show the varying geometries of the analytic model. The two spacecraft are shown as black dots. The enclosing black circle around each spacecraft bounds the area where a microburst will be observed by one or both AC6 units if the microburst's center lies inside the circle. Panel (A) shows the case where microburst diameter is smaller than the AC6 separation and all microbursts will be observed by either unit A or B and never simultaneously. Panel (B) shows the intermediate case where the microburst diameter is comparable to the AC6 separation and some fraction of microbursts will be observed simultaneously. The fraction of the microbursts simultaneously observed is proportional to the circle intersection area $A(r, s)$ and is shown with grey shading. Panel (C) shows the case where the microburst diameter is much larger than the spacecraft separation and nearly all microbursts will be observed by both spacecraft. Lastly panel (D) shows $\bar{F}(s)$ from the AC6 data with a solid black line, and modeled MC and analytic $\bar{F}(s)$ curves for a single-sized microburst distribution with $d = 40$ km.

uncertainty in the data is then propagated to θ which is then no longer an optimal value, rather a distribution of values that is consistent with the observations and its uncertainty.

Bayesian inference is rooted in Bayes theorem of conditional probability. Given the observed $\bar{F}(s)$ as y , and model's dependent variables as θ , Bayes theorem can be written as

$$p(\theta|y) = \frac{p(y|\theta)p(\theta)}{p(y)}. \quad (1.5)$$

$p(\theta)$ is the distribution of θ that describe our prior level of knowledge about that parameter e.g. from earlier microburst size studies, a microburst size must less than 500 km in LEO. This is called the prior which is quantified by a PDF such as normal, uniform, etc. Next term is the likelihood, $p(y|\theta)$, the conditional probability of obtaining y given a particular θ . The likelihood probability is a probabilistic penalty function that quantifies the discrepancy between the modeled and observed $\bar{F}(s)$ in terms of the standard error. The resulting PDF of θ s consistent with the observations is $p(\theta|y)$ known as the posterior distribution. The posterior is an update to our prior distributions, modified by the likelihood i.e. the data and its uncertainties. Here, the posterior is used to make inferences regarding the range of θ parameters that generate a $\bar{F}(s)$ that is consistent with the observations. The last parameter in Bayes theorem is $p(y)$. $p(y)$ is the marginal likelihood (evidence) that describes the probability of obtaining y after marginalizing over all prior variables. Calculation of $p(y)$ is difficult, and often not necessary for model parameter estimation.

With all of the above terminology, the important takeaway is that the posterior distribution for each model parameter is interpreted as the range of our model's dependent parameters that are consistent with the observations. A 95% credible

interval (CI) for each model parameter is reported here that is interpreted as:
 assuming a hypothesized $p(d|\theta)$, there is a 95% probability that the true θ is inside
 the CI. To sample the posterior distribution, the θ parameter space is explored with
 a Markov Chain Monte Carlo (MCMC) sampler. In a nutshell a Markov Chain is a
 process that samples random variables that depend on only the previous state of those
 random variables. Hence a MCMC sampler is a Monte Carlo sampler that samples
 the θ parameter space by picking random θ values based on the previous state of θ .

The first and one of the most popular MCMC is the Metropolis-Hastings
 sampler (Hastings, 1970; Metropolis et al., 1953). While the Metropolis-Hastings
 sampler is explained in detail in Metropolis et al. (1953) and Hastings (1970) and
 a good introduction given in Sambridge et al. (2006) as well as Sharma (2017), a
 brief overview is warranted. The Metropolis-Hastings sampler samples the posterior
 distribution in N trials. Once an initial set of θ is randomly picked from the prior,
 the i^{th} trial involves the following steps. First calculate the posterior probability for
 θ_i . Then pick a proposal θ_{i+1} to jump to, randomly picked near θ_i in parameter space.
 If the θ_{i+1} posterior probability is higher than θ_i , the MCMC accepts the proposal
 and moves to θ_{i+1} . If the posterior probability of θ_{i+1} is smaller than θ_i , there is a
 random chance that θ_{i+1} will be accepted or rejected (if rejected, $\theta_{i+1} = \theta_i$ and a
 new proposal is generated). This accept/reject criteria allows the sampler to trend
 to more probable θ while also exploring the neighboring regions. After the N trials,
 a histogram is made using the accepted θ s to produce the posterior distribution for
 each model parameter.

Estimating optimal parameters for various microburst size models

The MCMC sampler is first used to test the simplest microburst size model where
 all microbursts are one size and the MCMC will estimate that size. The microburst

size PDF for this model can be expressed as

$$p(d|d_0) = \delta(d - d_0) \quad (1.6)$$

where δ is the Dirac Delta function and d_0 is the diameter of all microbursts according to this model. The range of d that are consistent with the observed $\bar{F}(s)$ is shown in Fig. 1.6. Assuming this model, there is a 95% probability that the microburst diameter is between 38 and 129 km. As a sanity check the optimal size that minimizes least squares is 73 km.

A slight generalization of the one-size model is a two-size microburst population model that assumes the following microburst PDF

$$p(d|d_0, d_1, a) = a\delta(d - d_0) + (1 - a)\delta(d - d_1) \quad (1.7)$$

where the diameters of the two microburst populations are given by d_0 and d_1 and a is the parameter that quantifies the relative fractions of the two populations. The result of this model is shown in Fig. 1.7. The fit is slightly better than the one-size model, although that is to be expected given two more free model parameters. A majority, 98 %, of microbursts, have a diameter between 12 and 47 km with a rare population with a diameter between 76 and 234 km. The set of parameters that minimize least squares is 99.5 % of microbursts are small with a size of 21 km and the remaining 0.5 % of microbursts have a 140 km size.

Other, continuous PDFs were tested including: Maxwellian (Maxwell – Boltzmann), log-normal, and Weibull. The range of model parameters that are consistent with the observed $\bar{F}(s)$ are presented in the SI text S2. These distributions were chosen because they have the following properties that are most realistic: they are continuous, approach 0 in the limit as $r \rightarrow 0$ (lower bound microburst

size is ultimately limited by the electron gyroradius), and can be symmetrical or asymmetrical.

Discussion

The LEO microburst $\bar{F}(s)$ estimated in section 1 shows that a majority of coincident microbursts were observed by AC6 when they were separated by less than a few tens of km. This conclusion is consistent with prior literature and most similar to Parks (1967) who reported that many > 15 keV microbursts are less than 40 km in diameter while others were on average 80 ± 28 km in diameter. Furthermore, these results are similar to the bouncing packet example shown in Blake et al. (1996) with a size of “at least a few tens of kilometers”. The relatively small number of large > 70 km microbursts observed by AC6 fit in well with the results from Barcus et al. (1966) and Brown et al. (1965), although the AC6 separation is mostly latitudinal while Barcus et al. (1966) and Brown et al. (1965) used data from pairs of balloons separated predominantly in longitude.

Without knowledge of the microburst shape, a direct comparison between the AC6 and balloon observations is difficult. Trefall et al. (1966) discussed how a hypothetical circular microburst at the scattering location near the magnetic equator will be stretched into an ellipse with a semi-major axis in the longitudinal direction. This stretching effect should be explored further as it introduces an ambiguity from the eccentricity of the ellipse that prevents a direct latitudinal and longitudinal comparison.

When comparing our results to more recent studies, the AC6 microburst size distribution is much larger than the sizes reported in Dietrich et al. (2010) who used very low (VLF) frequency transmission paths and SAMPEX to conclude that microbursts must be smaller than 4 km from a small number of microbursts observed

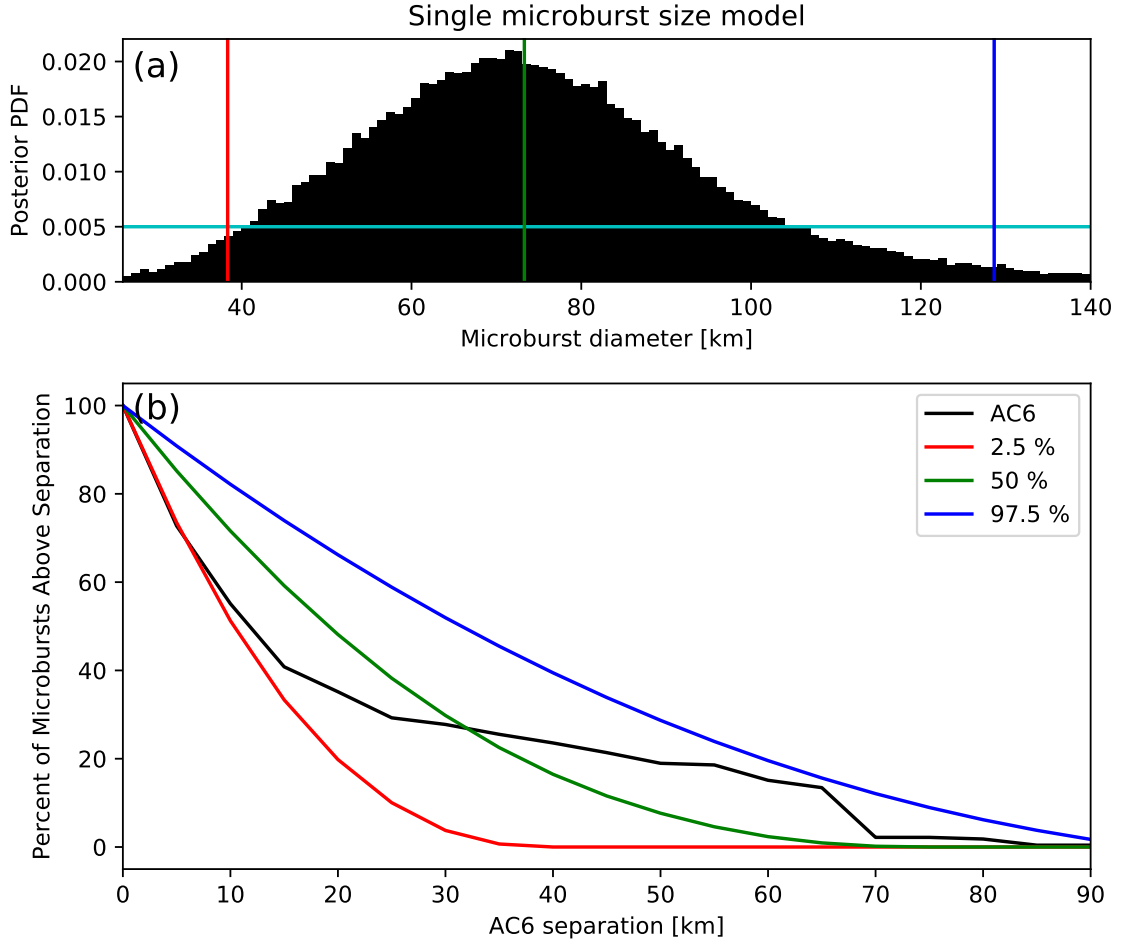


Figure 1.6: Range of plausible microburst sizes assuming all microbursts are one fixed size. Panel (a) shows the posterior probability density function of microburst diameters in black. The red, green, and blue vertical lines at 38, 73, and 129 km represent the 2.5, 50, and 97.5 posterior percentiles, respectively. A uniform prior between 0 and 200 km was assumed for this MCMC run and is shown in cyan. Panel (b) shows the percent of microbursts observed above an AC6 separation for $4 < L < 8$ in black. The 2.5, 50 and 97.5 size percentiles were estimated from the posterior and plotted in red, green, and blue curves, respectively.

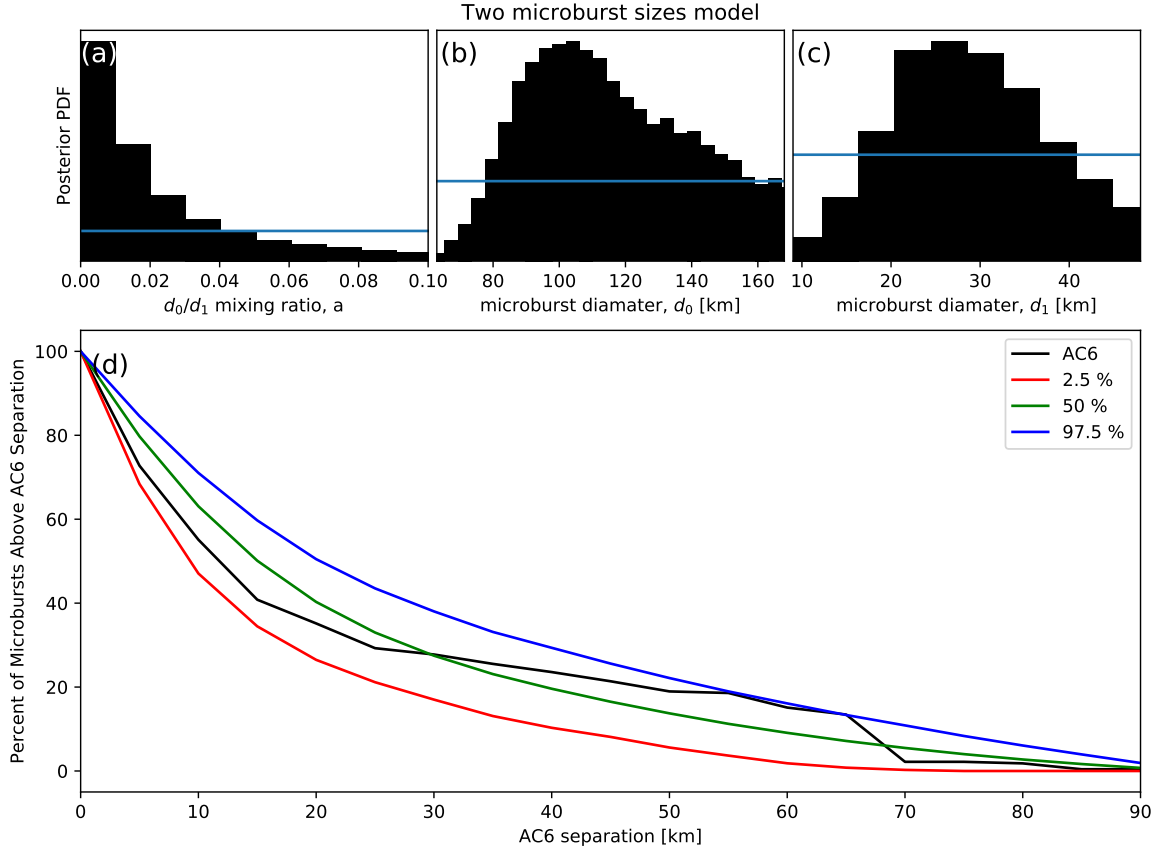


Figure 1.7: Plausible microburst percent curves assuming microburst size distribution is bimodal consisting of two sizes d_0 and d_1 with a mixing term that quantifies the relative occurrence of the d_0 to d_1 microburst populations. Panel (a) shows the posterior distribution for the microburst population mixing term, a with a median value of 0.02. The a prior was uniform between 0 and 0.2. Panel (b) shows the posterior distribution for d_0 , the larger microburst population estimated with a uniform prior between 50 and 200 km and the posterior median diameter of 122 km. Panel (c) shows the posterior distribution for d_1 , the smaller microburst population, estimated using a uniform prior between 0 and 50 km with a median diameter of 28 km. Panel (d) is similar to Fig. 1.6b and shows the AC6 microburst fraction for $4 < L < 8$ in black. A set of 1000 random parameter triples (a , d_0 , and d_1) were drawn from the posterior and used to generate a family of $\bar{F}(s)$ curves. At each s the range of consistent $\bar{F}(s)$ were quantified by the 2.5, 50 and 97.5 percentiles and shown with the red, green, and blue curves, respectively.

384 during one SAMPEX radiation belt pass. Dietrich et al. (2010) arrived at their
 385 conclusion by looking for temporal coincidence of microbursts and FAST events,
 386 subsecond VLF transmission perturbations, but the connection between FAST events
 387 and microbursts is not well understood. Lastly, our results are consistent with
 388 FIREBIRD-II observations of a > 11 km microburst reported by Crew et al. (2016),
 389 and the minority of microbursts observed by AC6 up to $s \approx 70$ km are consistent
 390 with the > 51 km bouncing packet microburst reported in Shumko et al. (2018).

391 The microburst PDF shown in Fig. 1.3b suggests that the microburst size
 392 distribution is bimodal. This has been suggested before by Blake et al. (1996) who
 393 noted that the > 150 keV and > 1 MeV microbursts are not always well correlated
 394 e.g. Fig. 10 in Blake et al. (1996). The quality of the AC6 data is insufficient to
 395 definitively conclude that there are two distinct microburst populations. The different
 396 microburst population hypothesis can be better tested with an AC6-like mission with
 397 better energy resolution and homogeneous MLT coverage.

398 The model results from section 1 emphasize that care must be taken when
 399 comparing the $\bar{F}(s)$ curves observed by AC6 and the true microburst size distribution
 400 due to the compounding effect of an unknown microburst size distribution, unknown
 401 microburst shape, and random microburst locations near AC6. By assuming there is
 402 only one microburst size, the results in Fig. 1.6 suggest that there is a 95% probability
 403 that the microburst diameter is somewhere between 38 and 129 km, a relatively wide
 404 range of values. On the other hand, the two-size model has a smaller variance around
 405 the AC6 $\bar{F}(s)$, which is expected with the addition of two more free parameters. The
 406 two size model is interpreted as 98% of microbursts diameters are between 12 and 47
 407 km and larger microbursts are very uncommon.

408 A variety of continuous $p(d)$ such as the Maxwellian, Weibull and log-normal
 409 were also tested. While the continuous microburst PDFs are more realistic, there is

no clear choice of which microburst PDF nature prefers. The one and two-size model are simple to interpret, and the two-size model qualitatively fits the observations the best out of all $p(d)$ tested. Surely nature does not only have two discrete microburst sizes. Rather, the current evidence and reasoning supports a bimodal and continuous PDF hypothesis. Due to lack of prior observations and theoretical predictions, it is difficult to identify and test a more appropriate $p(d)$ hypothesis at this time.

The equatorial microburst $\bar{F}(s)$ estimated in section 1 and Fig. 1.4b in particular shows that the majority of microbursts were observed when the equatorial AC6 separation was less than 200 km. We will now explore how these results compare to prior multi-point measurements of chorus source sizes made near the magnetic equator. The International Sun-Earth Explorers (ISEE 1 and 2) were used by Gurnett et al. (1979) to make one of the first direct chorus source scale measurements. Gurnett et al. (1979) estimated that the wave power correlation scale was on the order of a few hundred km across the background magnetic field. Using the Cluster Wide Band Data measurements Santolik et al. (2003) found the correlation scale of whistler mode chorus waves to be around 100 km near the source region at $L \approx 4$ and midnight MLT sector. Furthermore, Turner et al. (2017) used the four satellites comprising the Magnetospheric Multiscale Mission and found that rising tone whistler mode chorus elements were phase coherent up to 70 km at $L \approx 8$. Lastly, Agapitov et al. (2017, 2011, 2010, 2018) used multiple sets of spacecraft missions with wave measurements near the chorus source region to statistically show that the extent of chorus source region can extend from 600 km in the outer radiation belt to greater than 1,000 km in the outer magnetosphere.

The equatorial microburst size of less than a few hundred km shows that the waves responsible for scattering microburst electrons must have correlated properties on those scales. The wave properties necessary for scattering microburst electrons

e.g. coherence, polarization, wave normal angle, etc. can be identified by studying the waves properties that are only observed by multiple equatorial spacecraft at small separations. These properties can then aid wave-particle scattering model development by constraining the wave properties and scattering modes responsible for scattering microburst electrons. In turn, future models could then make predictions regarding the distribution of microburst sizes in LEO.

Conclusions

In conclusion, the twin AC6 CubeSats enabled the detailed statistical study of microburst sizes from a two point measurement platform. Roughly 60% of the > 35 keV microbursts were simultaneously observed while AC6 was separated by less than 20 km and the rest were observed up to ≈ 70 km separation. Modeling the microburst cumulative distribution function is essential to quantify the relationship between the number of microbursts observed as a function of separation to a hypothesized microburst size distributions. The AC6 microburst data, together with modeling, has hinted at the existence of a bimodal microburst size PDF with the majority of microbursts with a diameter smaller than 40 km and a rare microburst population with a diameter around 100 km. The bimodal size hypothesis may be more comprehensively addressed from LEO spacecraft with more simultaneous microburst observations, homogeneous MLT coverage, and differential energy channels. Moreover, to disentangle the compounding effect that affects two-point microburst measurements, a X-ray imager on a high altitude balloon can observe the atmospheric microburst footprint and determine the microburst size, shape, and any spatial correlations with little ambiguity.

When mapped to the magnetic equator, most microbursts were observed while the mapped AC6 separation was less than 200 km. This correlates well with the sizes

461 of highly correlated chorus waves and it suggests that the wave properties crucial for
462 scattering microbursts must be correlated over relatively small regions. By studying
463 the wave properties that are correlated on a few hundred km scales, the dominant
464 wave scattering modes may be identified.

465 Acknowledgments

466 This work was made possible with the help from the many engineers and
467 scientists at The Aerospace Corporation who designed, built, and operated AC6. M.
468 Shumko was supported by NASA Headquarters under the NASA Earth and Space
469 Science Fellowship Program - Grant 80NSSC18K1204. D.L. Turner is thankful for
470 support from the Van Allen Probes mission and a NASA grant (Prime award number:
471 80NSSC19K0280). Other Aerospace and MSU funding sources... The AC6 data is
472 available at <http://rbspgway.jhuapl.edu/ac6> and the IRBEM-Lib version used for this
473 analysis can be downloaded from <https://sourceforge.net/p/irbem/code/616/tree/>.

474

- 475 Abel, B. and Thorne, R. M. (1998). Electron scattering loss in earth's inner
 476 magnetosphere: 1. dominant physical processes. *Journal of Geophysical Research:*
 477 *Space Physics*, 103(A2):2385–2396.
- 478 Agapitov, O., Blum, L. W., Mozer, F. S., Bonnell, J. W., and Wygant, J. (2017).
 479 Chorus whistler wave source scales as determined from multipoint van allen probe
 480 measurements. *Geophysical Research Letters*, pages n/a–n/a. 2017GL072701.
- 481 Agapitov, O., Krasnoselskikh, V., Dudok de Wit, T., Khotyaintsev, Y., Pickett,
 482 J. S., Santolik, O., and Rolland, G. (2011). Multispacecraft observations of chorus
 483 emissions as a tool for the plasma density fluctuations' remote sensing. *Journal of*
 484 *Geophysical Research: Space Physics*, 116(A9):n/a–n/a. A09222.
- 485 Agapitov, O., Krasnoselskikh, V., Zaliznyak, Y., Angelopoulos, V., Le Contel, O.,
 486 and Rolland, G. (2010). Chorus source region localization in the earth's outer
 487 magnetosphere using themis measurements. *Annales Geophysicae*, 28(6):1377–
 488 1386.
- 489 Agapitov, O., Mourenas, D., Artemyev, A., Mozer, F., Bonnell, J., Angelopoulos, V.,
 490 Shastun, V., and Krasnoselskikh, V. (2018). Spatial extent and temporal correlation
 491 of chorus and hiss: Statistical results from multipoint themis observations. *Journal*
 492 *of Geophysical Research: Space Physics*, 123(10):8317–8330.
- 493 Anderson, K. A. and Milton, D. W. (1964). Balloon observations of X rays in the
 494 auroral zone: 3. High time resolution studies. *Journal of Geophysical Research*,
 495 69(21):4457–4479.
- 496 Barcus, J., Brown, R., and Rosenberg, T. (1966). Spatial and temporal character of
 497 fast variations in auroral-zone x rays. *Journal of Geophysical Research*, 71(1):125–
 498 141.
- 499 Blake, J., Looper, M., Baker, D., Nakamura, R., Klecker, B., and Hovestadt, D.
 500 (1996). New high temporal and spatial resolution measurements by sampex of the
 501 precipitation of relativistic electrons. *Advances in Space Research*, 18(8):171 – 186.
- 502 Blake, J. B. and O'Brien, T. P. (2016). Observations of small-scale latitudinal
 503 structure in energetic electron precipitation. *Journal of Geophysical Research:*
 504 *Space Physics*, 121(4):3031–3035. 2015JA021815.
- 505 Blum, L., Li, X., and Denton, M. (2015). Rapid MeV electron precipitation as
 506 observed by SAMPEX/HILT during high-speed stream-driven storms. *Journal of*
 507 *Geophysical Research: Space Physics*, 120(5):3783–3794. 2014JA020633.
- 508 Bortnik, J., Thorne, R., and Inan, U. S. (2008). Nonlinear interaction of energetic
 509 electrons with large amplitude chorus. *Geophysical Research Letters*, 35(21).

- 510 Boscher, D., Bourdarie, S., O'Brien, P., Guild, T., and Shumko, M. (2012). Irbem-lib
511 library.
- 512 Breneman, A., Crew, A., Sample, J., Klumpar, D., Johnson, A., Agapitov, O.,
513 Shumko, M., Turner, D., Santolik, O., Wygant, J., et al. (2017). Observations
514 directly linking relativistic electron microbursts to whistler mode chorus: Van allen
515 probes and FIREBIRD II. *Geophysical Research Letters*.
- 516 Brown, R., Barcus, J., and Parsons, N. (1965). Balloon observations of auroral zone
517 x rays in conjugate regions. 2. microbursts and pulsations. *Journal of Geophysical*
518 *Research (U.S.)*.
- 519 Crew, A. B., Spence, H. E., Blake, J. B., Klumpar, D. M., Larsen, B. A., O'Brien,
520 T. P., Driscoll, S., Handley, M., Legere, J., Longworth, S., Mashburn, K.,
521 Mosleh, E., Ryhajlo, N., Smith, S., Springer, L., and Widholm, M. (2016). First
522 multipoint in situ observations of electron microbursts: Initial results from the
523 NSF FIREBIRD II mission. *Journal of Geophysical Research: Space Physics*,
524 121(6):5272–5283. 2016JA022485.
- 525 Dietrich, S., Rodger, C. J., Clilverd, M. A., Bortnik, J., and Raita, T. (2010).
526 Relativistic microburst storm characteristics: Combined satellite and ground-based
527 observations. *Journal of Geophysical Research: Space Physics*, 115(A12).
- 528 Douma, E., Rodger, C. J., Blum, L. W., and Clilverd, M. A. (2017). Occurrence
529 characteristics of relativistic electron microbursts from SAMPEX observations.
530 *Journal of Geophysical Research: Space Physics*, 122(8):8096–8107. 2017JA024067.
- 531 Greeley, A., Kanekal, S., Baker, D., Klecker, B., and Schiller, Q. (2019). Quantifying
532 the contribution of microbursts to global electron loss in the radiation belts. *Journal*
533 *of Geophysical Research: Space Physics*.
- 534 Gurnett, D., Anderson, R., Scarf, F., Fredricks, R., and Smith, E. (1979). Initial
535 results from the isee-1 and-2 plasma wave investigation. *Space Science Reviews*,
536 23(1):103–122.
- 537 Hastings, W. K. (1970). Monte carlo sampling methods using markov chains and
538 their applications.
- 539 Horne, R. B. and Thorne, R. M. (2003). Relativistic electron acceleration and
540 precipitation during resonant interactions with whistler-mode chorus. *Geophysical*
541 *Research Letters*, 30(10). 1527.
- 542 Joy, S., Kivelson, M., Walker, R., Khurana, K., Russell, C., and Ogino, T. (2002).
543 Probabilistic models of the jovian magnetopause and bow shock locations. *Journal*
544 *of Geophysical Research: Space Physics*, 107(A10):SMP–17.

- Li, W., Thorne, R., Angelopoulos, V., Bonnell, J., McFadden, J., Carlson, C.,
LeContel, O., Roux, A., Glassmeier, K., and Auster, H. (2009a). Evaluation of
whistler-mode chorus intensification on the nightside during an injection event
observed on the THEMIS spacecraft. *Journal of Geophysical Research: Space
Physics*, 114(A1).
- Li, W., Thorne, R. M., Angelopoulos, V., Bortnik, J., Cully, C. M., Ni, B., LeContel,
O., Roux, A., Auster, U., and Magnes, W. (2009b). Global distribution of whistler-
mode chorus waves observed on the THEMIS spacecraft. *Geophysical Research
Letters*, 36(9). L09104.
- Lorentzen, K. R., Blake, J. B., Inan, U. S., and Bortnik, J. (2001a). Observations
of relativistic electron microbursts in association with VLF chorus. *Journal of
Geophysical Research: Space Physics*, 106(A4):6017–6027.
- Lorentzen, K. R., Looper, M. D., and Blake, J. B. (2001b). Relativistic electron
microbursts during the GEM storms. *Geophysical Research Letters*, 28(13):2573–
2576.
- Meredith, N., Horne, R., Summers, D., Thorne, R., Iles, R., Heynderickx, D., and
Anderson, R. (2002). Evidence for acceleration of outer zone electrons to relativistic
energies by whistler mode chorus. In *Annales Geophysicae*, volume 20, pages 967–
979.
- Metropolis, N., Rosenbluth, A. W., Rosenbluth, M. N., Teller, A. H., and Teller, E.
(1953). Equation of state calculations by fast computing machines. *The journal of
chemical physics*, 21(6):1087–1092.
- Millan, R. and Thorne, R. (2007). Review of radiation belt relativistic electron losses.
Journal of Atmospheric and Solar-Terrestrial Physics, 69(3):362 – 377.
- Mozer, F. S., Agapitov, O. V., Blake, J. B., and Vasko, I. Y. (2018). Simultaneous
observations of lower band chorus emissions at the equator and microburst
precipitating electrons in the ionosphere. *Geophysical Research Letters*.
- O’Brien, T. P., Blake, J. B., and W., G. J. (2016). Aerocube-6 dosimeter data readme.
Technical Report TOR-2016-01155, The Aerospace Corporation.
- O’Brien, T. P., Looper, M. D., and Blake, J. B. (2004). Quantification of relativistic
electron microburst losses during the GEM storms. *Geophysical Research Letters*,
31(4). L04802.
- O’Brien, T. P., Lorentzen, K. R., Mann, I. R., Meredith, N. P., Blake, J. B., Fennell,
J. F., Looper, M. D., Milling, D. K., and Anderson, R. R. (2003). Energization of
relativistic electrons in the presence of ULF power and MeV microbursts: Evidence
for dual ULF and VLF acceleration. *Journal of Geophysical Research: Space
Physics*, 108(A8).

- Olson, W. P. and Pfitzer, K. A. (1982). A dynamic model of the magnetospheric magnetic and electric fields for July 29, 1977. *Journal of Geophysical Research: Space Physics*, 87(A8):5943–5948.
- Parks, G. K. (1967). Spatial characteristics of auroral-zone X-ray microbursts. *Journal of Geophysical Research*, 72(1):215–226.
- Sambridge, M., Gallagher, K., Jackson, A., and Rickwood, P. (2006). Trans-dimensional inverse problems, model comparison and the evidence. *Geophysical Journal International*, 167(2):528–542.
- Santolik, O., Gurnett, D., Pickett, J., Parrot, M., and Cornilleau-Wehrin, N. (2003). Spatio-temporal structure of storm-time chorus. *Journal of Geophysical Research: Space Physics*, 108(A7).
- Sharma, S. (2017). Markov chain monte carlo methods for bayesian data analysis in astronomy. *Annual Review of Astronomy and Astrophysics*, 55:213–259.
- Shumko, M., Sample, J., Johnson, A., Blake, B., Crew, A., Spence, H., Klumpar, D., Agapitov, O., and Handley, M. (2018). Microburst scale size derived from multiple bounces of a microburst simultaneously observed with the firebird-ii cubesats. *Geophysical Research Letters*, 45(17):8811–8818.
- Thorne, R. M., O’Brien, T. P., Shprits, Y. Y., Summers, D., and Horne, R. B. (2005). Timescale for MeV electron microburst loss during geomagnetic storms. *Journal of Geophysical Research: Space Physics*, 110(A9). A09202.
- Trefall, H., Bjordal, J., Ullaland, S., and Stadsnes, J. (1966). On the extension of auroral-zone x-ray microbursts. *Journal of Atmospheric and Terrestrial Physics*, 28(2):225–233.
- Tsurutani, B. T., Lakhina, G. S., and Verkhoglyadova, O. P. (2013). Energetic electron (~ 10 keV) microburst precipitation, ~ 5 –15 s x-ray pulsations, chorus, and wave-particle interactions: A review. *Journal of Geophysical Research: Space Physics*, 118(5):2296–2312.
- Turner, D., Lee, J., Claudepierre, S., Fennell, J., Blake, J., Jaynes, A., Leonard, T., Wilder, F., Ergun, R., Baker, D., et al. (2017). Examining coherency scales, substructure, and propagation of whistler mode chorus elements with magnetospheric multiscale (mms). *Journal of Geophysical Research: Space Physics*, 122(11).
- Van Allen, J. A. (1959). The geomagnetically trapped corpuscular radiation. *Journal of Geophysical Research*, 64(11):1683–1689.
- Vernov, S. and Chudakov, A. (1960). Investigation of radiation in outer space. In *International Cosmic Ray Conference*, volume 3, page 19.

- 618 Woodger, L., Halford, A., Millan, R., McCarthy, M., Smith, D., Bowers, G., Sample,
619 J., Anderson, B., and Liang, X. (2015). A summary of the BARREL campaigns:
620 Technique for studying electron precipitation. *Journal of Geophysical Research:*
621 *Space Physics*, 120(6):4922–4935.